Frictiotaxis underlies adhesion-independent durotaxis

Adam Shellard[1*], Kai Weißenbruch[1*], Peter A. E. Hampshire[2,3], Namid R. Stillman[1], Christina L. Dix[4], Richard Thorogate[5], Albane Imbert[4], Guillaume Charras[1,5], Ricard Alert[2,3,6,**], Roberto Mayor[1,7,**].

[1]*Department of Cell and Developmental Biology, University College London, Gower Street, London, WC1E 6BT, UK*

[2]*Max Planck Institute for the Physics of Complex Systems, Nöthnitzerst. 38, 01187, Dresden, Germany*

[3]*Center for Systems Biology Dresden, Pfotenhauerst. 108, 01307, Dresden, Germany*

[4]*The Francis Crick Institute, 1 Midland Road, London, NW1 1AT, UK*

[5]*London Centre for Nanotechnology, University College London, London, WC1H 0AH, UK*

[6]*Cluster of Excellence Physics of Life, TU Dresden, 01062, Dresden, Germany*

[7]*Center for Integrative Biology, Faculty of Sciences, Universidad Mayor, Santiago, Chile*

* Co-first authors

** Corresponding authors: R.A. (Email: ralert@pks.mpg.de), R.M. (Email: r.mayor@ucl.ac.uk)

Cells move directionally along gradients of substrate stiffness, a process called durotaxis. The current consensus is that durotaxis relies on cell-substrate focal adhesions to sense stiffness and transmit forces that drive directed motion. Therefore, focal adhesion-independent durotaxis is thought to be impossible. Here, we show that confined cells can perform durotaxis despite lacking strong or specific adhesions. This durotactic migration depends on asymmetric myosin distribution and actomyosin retrograde flow. We show that the mechanism of this adhesion-independent durotaxis is that stiffer substrates offer higher friction. We propose a physical model that predicts that non-adherent cells polarise and migrate towards regions of higher friction – a process that we call frictiotaxis. We demonstrate frictiotaxis in experiments by showing that cells migrate up a friction gradient even when stiffness is uniform. Our results broaden the potential of durotaxis to guide any cell that contacts a substrate and reveal a new mode of directed migration based on friction, with implications for immune and cancer cells, which commonly move with non-specific interactions.

The ability of cells to migrate following environmental gradients underlies many aspects of development, homeostasis and disease[1,2]. Cells follow gradients in the stiffness of their substrate, a process called durotaxis that has been demonstrated in multiple cell types *in vitro* and *in vivo*[3-7]. The prevailing mechanistic view of durotaxis involves the cells' actomyosin machinery producing contractile forces that pull on the underlying substrate through focal adhesions. These pulling forces then bias cell motion in one direction, typically toward the stiffer substrate[5,8-10]. These physical models are supported by experimental evidence, and an essential component of all of them is strong cell-substrate adhesions. It is thus believed that cells lacking adhesions must be incapable of sensing stiffness gradients. Whether cells lacking cell-matrix adhesions can respond to mechanical gradients is widely acknowledged as a vital question[11-14] that has been unaddressed. Its importance is highlighted by the fact that adhesion-independent motility is a fundamental mode of migration, classically exhibited by various cancer and immune cells, but which can be triggered in practically any cell type by providing 3D confinement[15,16].

Microchannels with tuneable stiffness

Part of the challenge in addressing whether cells migrating without adhesions are capable of responding to stiffness gradients, or indeed the role of substrate stiffness in the context of 3D adhesion-independent motility in general, lies in the technical challenge of fabricating confined cellular environments of tuneable stiffness that are necessary to study adhesion-independent migration[12]. Adhesion-independent motility has commonly been studied using the 'under agarose assay' in which cells emigrate from a free region into confinement between agarose and glass. However, this method is unable to differentiate between the effect of confinement and the effect of compression since cells must deform their substrate to move. A newer method uses microchannels fabricated with polydimethylsiloxane (PDMS). However, this material exhibits stiffness in the MPa range, far from physiologically relevant

levels of most tissues, and offers little ability to tune rigidity. We developed a novel and easy-to-use method in which mobile and deformable cells spontaneously migrate into and within agarose-surrounded preformed microchannels (Fig. 1a). Fabricating microchannels with agarose offers the potential to investigate cells within substrates of physiologically relevant stiffnesses[17]. The dimensions of the channel are determined by a PDMS mould that provides reliable confinement irrespective of microchannel dimensions (Fig. 1b,c and Extended Data Fig. 1a-c) and is unaffected by the stiffness of the substrate (Fig. 1e,g and Extended Data Fig. 1d,e). The stiffness of the microchannel is tuned by the concentration of agarose (Fig. 1d). Fluorospheres did not show directed motion within microchannels (Extended Data Fig. 1f,g), confirming that pressure-driven fluid flow was not a factor in this setup. Importantly, stiffness gradients can be created by combining solutions with different agarose concentrations together during microchannel assembly (Fig. 1h,i).

To test our setup as a valid means of assaying confined non-adherent cellular motility, we used a non-adherent subline of Walker 256 carcinosarcoma (henceforth Walker) cells as a well-validated model of a cell type that moves without using specific substrate adhesions and without focal adhesions[18,19]. Although Walker cells are able to attach to fibronectin, they are completely non-adhesive on agarose or on glass coated with PLL-PEG (Fig. 2a,b, Extended Data Fig. 2). Furthermore, Walker cells introduced into the agarose microchannel setup exhibited classical amoeboid motion characterised by bleb-based rather than lamellipodium-based motility (Fig. 2c,d and Supplementary Video 1), fast migration (Fig. 2e) and lack of focal adhesions (Fig. 2f,g). Together, these observations indicate that Walker cells are non-adhesive in our agarose microchannel setup.

Adhesion-independent durotaxis

82 To directly address whether cells are capable of undergoing durotaxis in an adhesion-
83 independent manner, agarose microchannels were fabricated to have either uniform stiffness
84 or a stiffness gradient (Fig. 3a). We tracked migratory cells that entered regions of the
85 microchannel which exhibited either uniform or graded stiffness. Cells entering substrate of
86 uniform stiffness had a moderate tendency to repolarise and move back, whereas cells
87 entering a stiffness gradient were characterised by much higher persistence as they migrated
88 toward the stiff substrate (Fig. 3b-e and Supplementary Video 2). In addition, cells exhibited
89 a higher migration speed at higher stiffness values (Fig. 3f and Extended Data Fig. 3). Like
90 Walker cells, HL60 neutrophil-like cells, a cell type with a well-described amoeboid
91 behaviour[20], also exhibited preferred motion toward stiffer substrate (Extended Data Fig. 4).
92 Together, these results reveal adhesion-independent durotaxis may be a generalisable
93 phenomenon.

94 **Ameboid durotaxis depends on actomyosin flow**

95 It has previously been described that amoeboid migration on substrates of uniform stiffness
96 depends on actomyosin retrograde flow[18]. We therefore asked whether actomyosin retrograde
97 flow was also observed in our cells undergoing adhesion-independent durotaxis. Walker cells
98 expressing myosin-GFP were placed in the agarose microchannels with either uniform
99 stiffness or a stiffness gradient, followed by time-lapse imaging. Cells exhibited an
100 accumulation of myosin at the rear and a clear myosin retrograde flow (Fig. 4a,b, Extended
101 Data Fig. 5a-c and Supplementary Video 4&5). Upon cell repolarisation, the direction of
102 retrograde actomyosin flow was reversed, leading to accumulation of actomyosin at the new
103 cell rear (Fig. 4b and Supplementary Video 4). A clear positive correlation between
104 actomyosin flow and cell speed was observed (Fig. 4c and Extended Data Fig 5c). To
105 determine whether myosin was required for adhesion-independent durotaxis, myosin activity
106 was reduced by treating cells with the ROCK inhibitor Y-27632. A clear loss in the rear

107 accumulation of myosin (Fig. 4d), retrograde flow (Extended Data Fig 5d), bleb formation
108 (Fig. 4g), and impairment of migration was observed in treated cells compared with control
109 cells (Fig. 4e,f,h and Supplementary Video 6). These observations show that rear
110 accumulation of myosin dependent on actomyosin retrograde flow is required for adhesion-
111 independent durotaxis.

112 **An active gel model of amoeboid migration predicts frictiotaxis**

113 Given that amoeboid cells lack focal adhesions, it was unclear how these cells were able to
114 durotax. We hypothesised that regions of higher stiffness may offer higher friction, which
115 arises from non-specific molecular interactions between the cell membrane and the channel
116 walls[18]. We also hypothesised that, in the absence of active forces pulling the substrate, this
117 passive friction would cause amoeboid cells to undergo durotaxis.

118 We investigated this hypothesis through a physical model of amoeboid motility which treats
119 the actomyosin network in the cell cortex as an active gel[13,15,16,18,21-25]. In this model, myosin-
120 generated contractility triggers an instability whereby the gel concentrates towards one side,
121 which becomes the cell rear (Fig. 5a). This concentration profile drives retrograde
122 actomyosin flow, which propels the cell forward. In the absence of external gradients,
123 symmetry is broken spontaneously. The cell can thus move either left or right (Fig. 5a),
124 consistent with our experimental observations of repolarisation events in uniform channels
125 (Fig. 3c,d).

126 To benchmark this model, defined by Eqs. S13-S16 in the Supplementary Note, we solved it
127 numerically and obtained the steady-state actomyosin concentration profile (Methods). This
128 profile fits the experimentally measured profile of myosin intensity (Extended Data Fig. 6-7,
129 Table I, see Methods), which shows that the model captures the myosin-driven amoeboid
130 migration in our experiments.

Within the framework of this model, we next asked what would happen if the cells were exposed to an external friction gradient. We show that, in the model, a friction gradient can break the symmetry and yield migration toward regions of higher friction. Starting from an unpolarised state with uniform gel concentration, contractile stresses from the cell poles generate faster cortex flows in low-friction areas. These flows concentrate the gel towards the low-friction side, which thus becomes the cell rear (Fig. 5b).

To demonstrate this mechanism of symmetry breaking, we considered force balance for the actomyosin gel:

$$\xi \phi v = \frac{\mathrm{d}\sigma}{\mathrm{d}x}. \tag{1}$$

The left-hand side represents gel-substrate friction, which is proportional to the coefficient $\xi(x)$, the volume fraction $\phi(x)$ of the gel, and its velocity $v(x)$ with respect to the substrate. The right-hand side represents the forces generated within the gel. These forces arise from gradients of the gel stress $\sigma = \sigma_a + \sigma_v - \Pi$, which includes contributions from active contractility, $\sigma_a = \zeta\phi$, gel viscosity $\sigma_v = \eta\phi\ \mathrm{d}v/\mathrm{d}x$, and osmotic pressure $\Pi = \alpha(\phi - \phi_0)^3 - \gamma\ \mathrm{d}^2\phi/\mathrm{d}x^2$[24]. Here, ζ, η, α, and γ are material parameters described in more detail in Reference[24] and in the Supplementary Note, and ϕ_0 is the equilibrium volume fraction of the gel.

Because the cell poles are not subject to substrate friction, they undergo the contractile instability earlier and faster than the rest of the gel. The resulting pole contraction pulls in gel from the central region of the cell (Fig. 5b). In the central region, the gel starts in the unpolarised state with uniform gel concentration $\phi(x) = \phi_0$, for which the force balance Eq. (1) reduces to

$$\xi v = \eta \frac{\mathrm{d}^2 v}{\mathrm{d}x^2}. \tag{2}$$

To capture the mechanism of symmetry breaking, we solve this force balance close to the two ends of the central region, which are subject to a stress σ_{pole} arising from pole contraction and have different friction coefficients ξ_- and ξ_+, with $\xi_- < \xi_+$. Thus, we obtain the velocities of the two ends, v_+ and v_- (Supplementary Note):

$$v_\pm = \pm \frac{\sigma_{pole}}{\sqrt{\eta\, \xi_\pm}}. \tag{3}$$

As illustrated in Fig. 5b, this result shows that the gel flows faster towards the pole in the low-friction region, which leads to gel accumulation towards that side and subsequent cell migration towards high-friction regions.

Overall, our theory predicts a mode of cell migration guided by friction gradients (Fig. 5b), which we call frictiotaxis. These results suggest that cells without strong focal adhesions perform durotaxis by exploiting gradients in friction rather than stiffness variations.

Substrate friction and stiffness are correlated

To test this idea in experiments, we first probed the relationship between stiffness and friction by performing lateral force microscopy (LFM) on the agarose microchannels across the stiffness range in which we observed durotaxis. LFM measures the torsional deformation of the micro-mechanical cantilever of an atomic force microscope during contact mode, enabling the measurement of frictional properties. We found that, in accordance with our hypothesis, stiffer substrates exhibited higher friction forces (Fig. 6a).

Experimental evidence of frictiotaxis

If amoeboid durotaxis is based on friction, it should be impaired if the channel walls are passivated with polyethylene glycol (PEG), which has been shown to provide low-friction substrates[18,26] (Fig. 6b). Additionally, cells should be capable of directed migration when stiffness is uniform, but friction is graded.

179 To test the first prediction, we employed a previously described method in which agarose is
180 coupled to proteins after the surface is activated with cyanogen bromide, enabling functional
181 interactions between the cell and the coated surface[27,28]. As a proof of principle, cells adhered
182 strongly to fibronectin-coated agarose gels (Extended Data Fig. 8a). We thus coated agarose
183 microchannels exhibiting a stiffness gradient with PLL-g-PEG (Extended Data Fig. 8b,c).
184 Cells migrating through such channels had impaired durotaxis, compared to controls (Fig. 6c-
185 e). Thus, durotaxis is impaired by a reduced friction despite the presence of a stiffness
186 gradient.

187 To address whether gradients in friction are sufficient to guide cell migration in the absence
188 of adhesions, we generated gradients in friction by micropatterning gradients of bovine serum
189 albumin (BSA), which provides high friction, and PEG, which provides low friction[18], onto
190 glass and within PDMS microchannels (Fig. 6f,h and Extended Data Fig. 8d,e), such that
191 regions without BSA contained PEG. By performing LFM, we validated that BSA-coated
192 regions provided higher friction than PEG-coated regions (Fig. 6b), which supports previous
193 evidence[18]. We observed cells moving toward areas of higher friction when they migrated in
194 these channels, as opposed to randomly directed motion when friction was uniform (Fig. 6h-j
195 and Supplementary Video 7). Motion guided by friction gradients was previously
196 conceptualized[29] and demonstrated in magnetic colloidal particles[30]. Here, our experimental
197 data confirm that cells perform frictiotaxis, and they suggest that this mode of directed
198 migration provides the mechanism for adhesion-independent durotaxis.

199 **Discussion**

200 Altogether, our study contributes to the growing field questioning how the physical
201 environment modulates adhesion-independent migration[22,31,32]. Our results reveal that strong
202 and specific adhesions are redundant for durotaxis thanks to non-specific friction forces,

203 which enable preferential movement toward stiffer substrates because stiffness and friction
204 are correlated. In practice, different tissues may exhibit different stiffness-friction
205 relationships, thus affecting cell response. Although cells performing amoeboid migration
206 might have weak adhesions, the mechanism of directed motion that we reveal is entirely
207 based on friction. Accordingly, our model includes no adhesion, i.e., no resistance to normal
208 pulling forces, but just friction that opposes cell-substrate sliding.

209 Modulating only one physical variable, in this case stiffness, to investigate cell behaviour is a
210 major challenge. Despite establishing the dominant role of friction, we cannot rule out that
211 differential substrate deformation contributes to adhesion-independent durotaxis. In this
212 study, we used microchannels that were larger than the nucleus, because amoeboid cells use
213 the nucleus as a mechanical gauge in path-making decisions[33]. We also chose to use pre-
214 formed paths, rather than an 'under agarose assay', to rule out the role of compression on the
215 cells, since cells under compression must physically deform their surroundings to move,
216 which is more difficult when the substrate is stiffer[31]. Whether cell compression and other
217 physical inputs can act as guidance cues for adhesion-independent cell motility remains an
218 open question. Notably, however, geometric patterns can guide adhesion-independent
219 motility[22,34].

220 Finally, whether frictiotaxis and amoeboid durotaxis are physiologically relevant in the
221 complex *in vivo* environment, especially considering that chemotactic signals are extremely
222 potent drivers of directional cell migration, is also unknown. A promising candidate are
223 immune cells, which often need to traverse tissues of high density to reach target sites.
224 Adhesion-independent durotaxis could contribute significantly to this type of directed
225 migration.

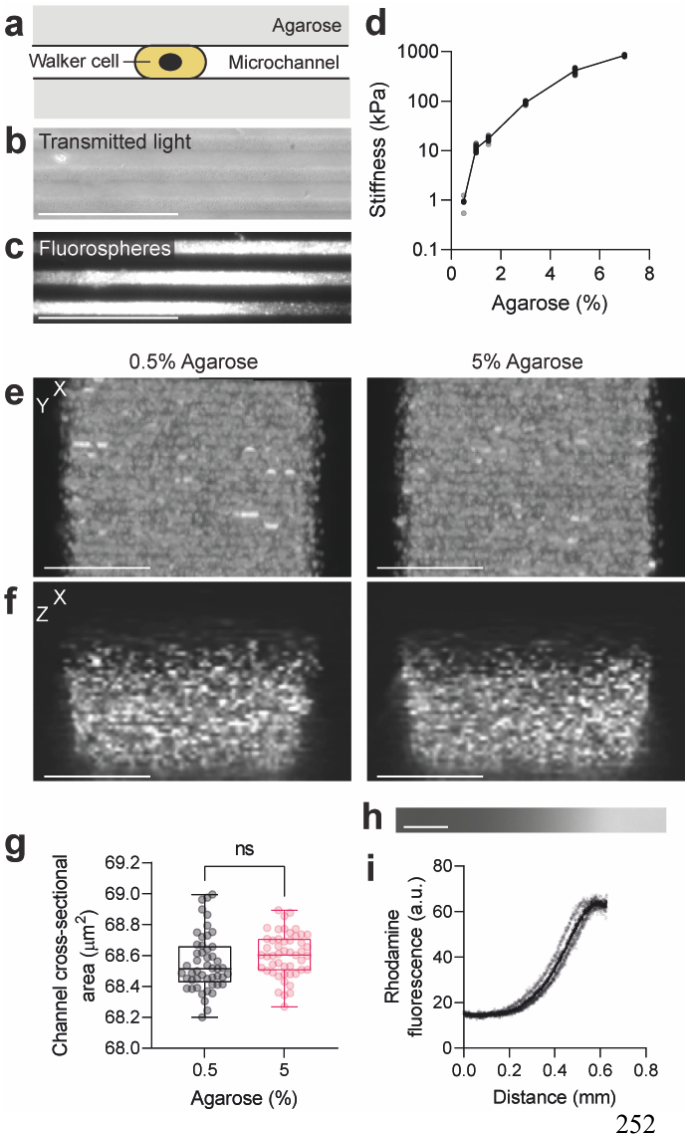

Figure 1. A microchannel system with tuneable stiffness and dimensions. a, Diagram of the microchannel assay. Microchannel dimensions determine the geometry of the setup and the agarose surrounding the cell determines substrate stiffness. **b-c**, Agarose channels (**b**) filled with 0.2 µm fluorospheres (**c**). Scale bar, 100 µm. **d**, Stiffness measurements (mean ± s.d.) by nanoindentation of gels of different agarose concentration. Grey dots represent individual data points, black dots represent mean. n = 25 cells. **e-g**, Agarose microchannels (**e-f**; 0.5%, left; 5%, right) filled with 0.2 µm fluorospheres and imaged from below (**e**, maximum projection) and side-on (**f**). Channel cross-sectional area quantified (**g**). Scale bar, 5 µm. For **g**, n = 49 channels; unpaired two-tailed t test; ns, P>0.05 (exact: P=0.2229). **h-i**, A stiffness gradient visualized by immersing rhodamine dextran dye into one of the agarose solutions prior to subsequent diffusion and solidification (**h**) and quantification of the dye fluorescence over the gradient axis (**i**). Scale bar, 100 µm. Grey dots represent individual data points, black dots represent mean. n = 5 gels.

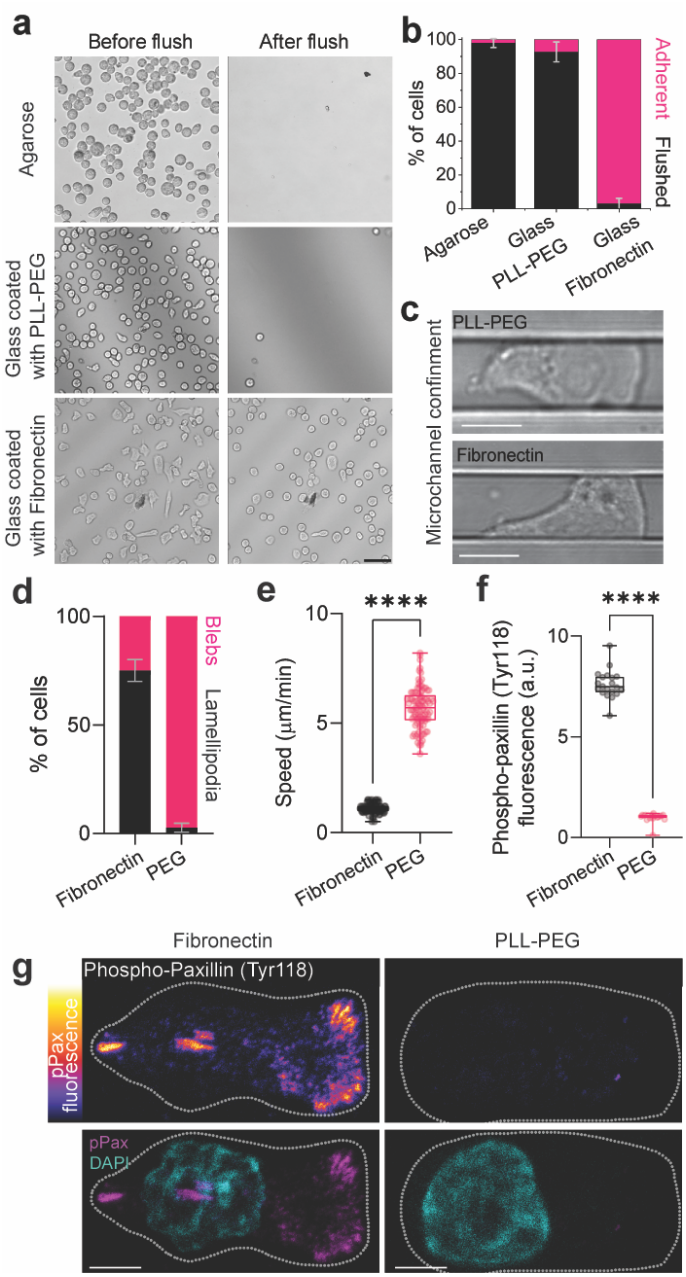

Figure 2. Walker cells exhibit adhesion-independent amoeboid migration in the microchannel system. a, Images of Walker cells on agarose, glass coated with PLL-PEG, and glass coated with fibronectin, before and after flushing the substrate with culture medium. Scale bar, 50 µm. **b**, Quantification of adherent and flushed fraction of cells after flushing the respective substrates. Bars represent mean ± s.d.; $N = 3$ experimental repeats. **c**, Example images of cells in non-adhesive (PLL-PEG, top) or adhesive (fibronectin, bottom) agarose microchannels. Scale bar, 10 µm. **d**, Quantification of lamellipodia and blebs by cells in adhesive (fibronectin) and non-adhesive (PEG) conditions. Bars represent mean ± s.d.; $N = 3$ experimental repeats. **e,** Speed of cells migrating within agarose microchannels with fibronectin or PEG coating. **f-g**, Immunostaining against phospho-paxillin (Tyr118) in Walker cells within agarose channels (**g**) and quantification (**f**) in which the underlying glass is coated with either PLL-PEG or fibronectin. Dotted white line represents the cell outline. Scale bar, 5 µm. $n = 100$ cells (**e, f**); two-tailed Mann-Whitney test; ****$P \leq 0.0001$.

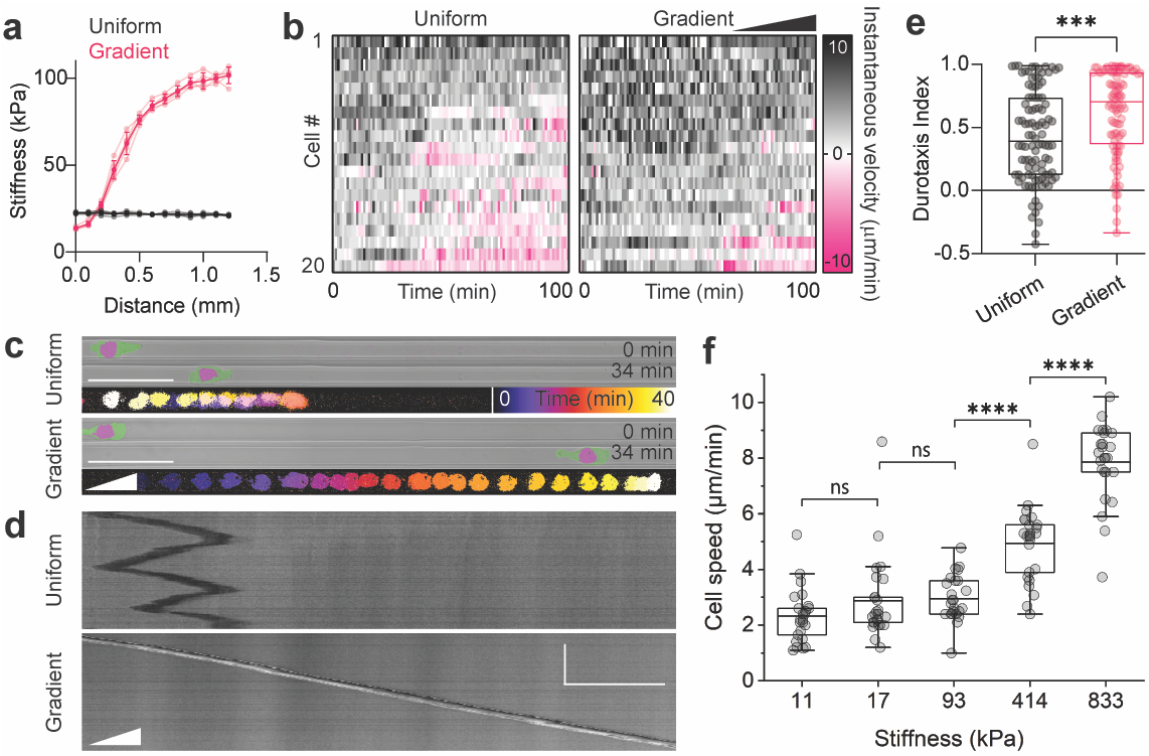

Figure 3. Adhesion-independent durotaxis of Walker cells. a, Stiffness measurements (mean ± s.d.) from nanoindentation of uniform (black) and gradient (pink) microchannels. Opaque dots and lines represent mean; translucent dots and lines represent raw data. $n = 5$ gels each. **b**, Heat maps of the instantaneous velocity of representative cells migrating within microchannels of uniform or graded stiffness. $n = 20$ representative cells each. Each row represents a different cell. The x-axis represents time, with each box representing 1 min for a total of 100 min. Each heat map is ordered such that cells migrating forward (black) are at the top, and cells migrating backwards (pink) are at the bottom. **c**, Example pictures of cells at an earlier (top panels) and later (middle panels) time point, and temporal colour-coded projected tracks (bottom panels). Cells are tracked by a nuclear marker and membrane is pseudocoloured. Scale bar, 50 µm. **d**, Kymographs of the cells shown in (**c**). Scale bar, 50 µm (horizontal), 50 min (vertical). **e**, Quantification of durotaxis. $n = 100$ cells; two-tailed Mann-Whitney test; ***$P \leq 0.001$ (exact: $P = 0.0003$). **f**, Quantification of migration speed in microchannels of different stiffness regimes. $n = 25$ cells for each stiffness regime; two-tailed Mann-Whitney test; ns, $P > 0.05$ (11 versus 17: $P = 0.23258$; 17 versus 93: $P = 0.09795$), ****$P \leq 0.0001$.

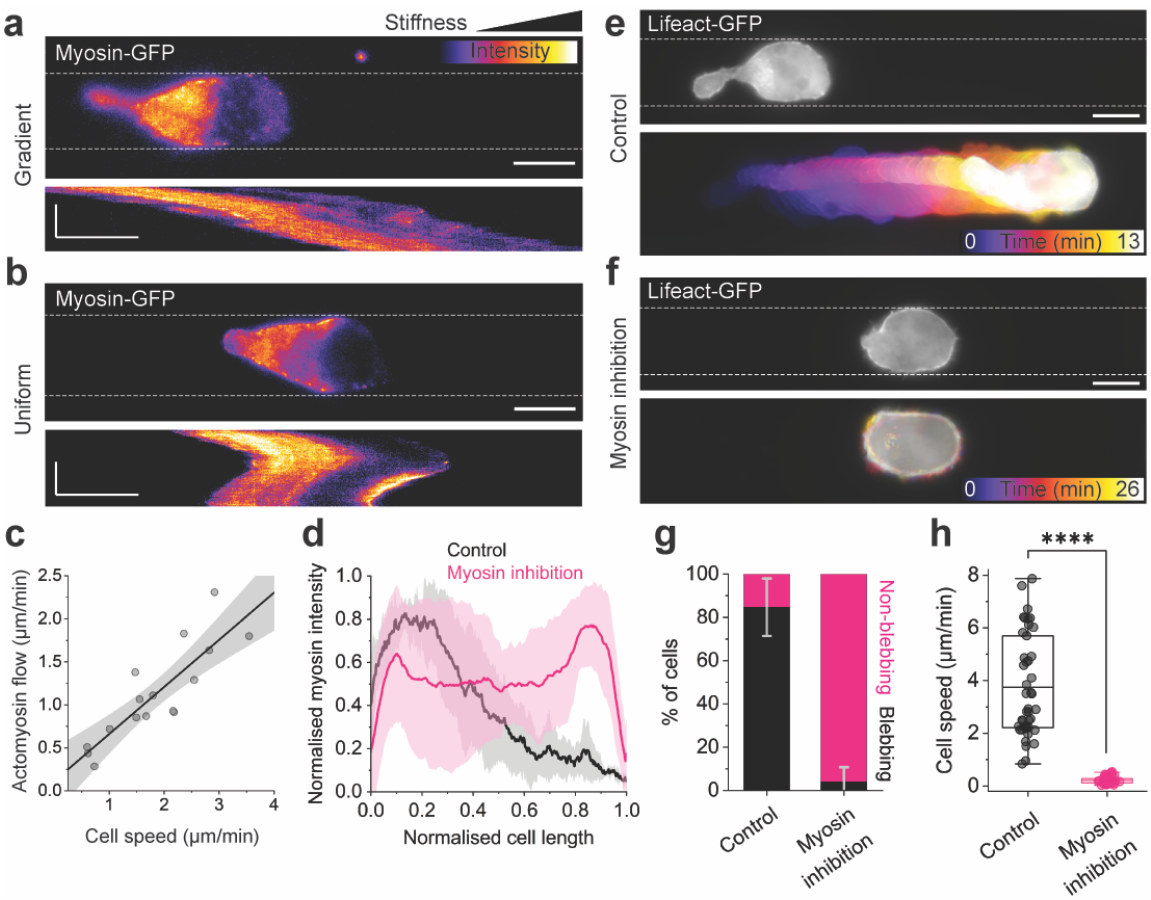

Figure 4. Adhesion-independent durotaxis depends on retrograde actomyosin flow. a-b, Still images and corresponding kymographs from timelapse records of Myosin-GPF-expressing Walker cells, migrating in microchannels with stiffness gradient (**a**) or uniform stiffness (**b**). Fluorescence signal was colour-coded, dotted lines represent channel boundaries. Scale bars, 10 µm in still images, 5 µm (horizontal) and 10 min (vertical) in kymographs. **c**, Correlation of actomyosin flow and migration speed. Coefficient of determination (R^2) = 0.73068. Grey areas depict upper and lower 95% confidence limits. Dots represent mean values of individual cells migrating over 400 s. Data points of n = 8 cells in stiffness gradients or uniform stiffness were picked randomly from N = 3 independent experiments each and pooled. **d**, Intensity profiles of Myosin-GFP signals along the front-rear axis of Walker cells in the absence (DMSO control, black line) or presence of 30 µM Y-27632 (Myosin inhibition, purple line). Myosin-GFP intensity and cell length were normalised for comparison. Solid lines plus transparent areas depict mean ± s.d. of n = 6 cells each, from N=3 independent experiments. **e-f**, Still images and corresponding colour-coded timelapse records of Lifeact-GPF-expressing Walker cells in microchannels of uniform stiffness; in the absence (**e**) or presence of 30µM Y-27632 (**f**). Dotted lines represent channel boundaries. Scale bars, 10 µm. **g**, Quantification of blebbing and non-blebbing fractions of cells under control (DMSO) or myosin inhibiting (30 µM Y-27632) conditions. Bars represent mean ± s.d. from N = 3 independent experiments. **h**, Quantification of migration speed in microchannels of uniform stiffness. n = 43 cells for control (DMSO) and n = 47 cells for myosin inhibition (30 µM Y-27632); two-tailed Mann-Whitney test; ****$P \leq 0.0001$.

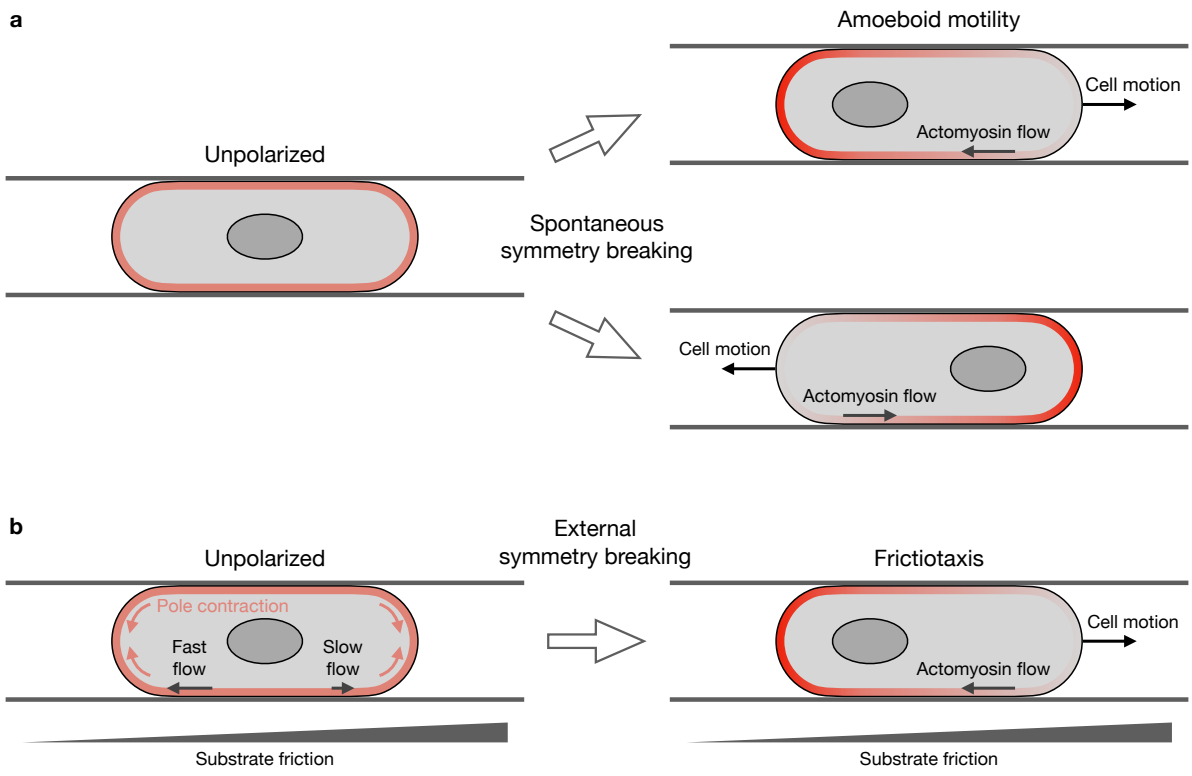

Figure 5. Model of frictiotaxis. a, In the absence of external gradients, unpolarised cells break symmetry spontaneously and display amoeboid motility either left or right. **b**, On a friction gradient, contractile stresses from the poles produce faster cortical flows on the lower-friction side. These flows break the symmetry and accumulate actomyosin towards the low-friction side, which drives frictiotaxis, that is directed cell migration towards higher friction.

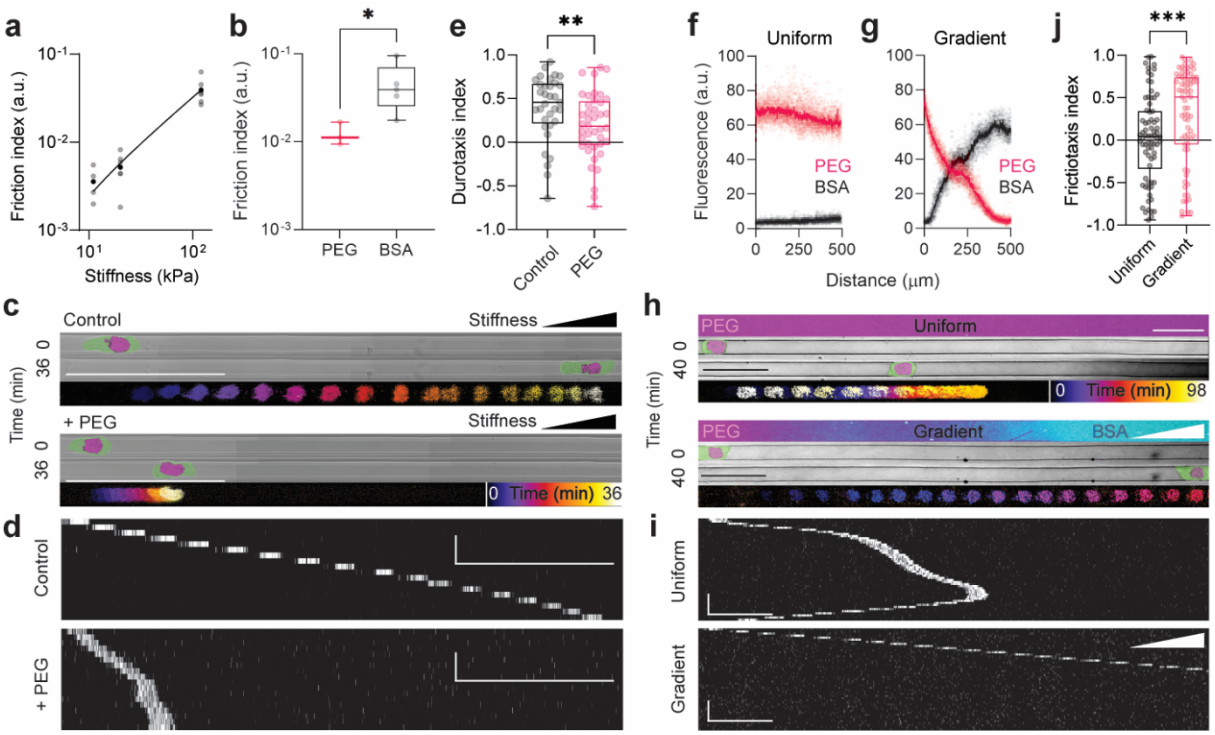

Figure 6. Friction-driven directed migration. a, Friction index versus stiffness in the gels; $n = 4$ (*in vitro*, at 11 kPa); $n = 6$ (*in vitro*, other stiffness values). **b**, Friction of PEG- or BSA-treated glass; $n = 3$ (PEG); $n = 5$ (BSA); two-tailed Mann-Whitney test; $^{*}P \leq 0.05$ (exact: $P = 0.0357$). **c**, Pictures of Walker cells with a nuclear label and pseudocoloured membrane after t=0 min and t=36 min in stiffness-gradient microchannels without (Control, upper panel) or with PLL-PEG coating (+ PEG, lower panel). Temporal colour-coded projected tracks of the nucleus are shown in the bottom of each of the panels. Scale bars, 100 µm. **d**, Kymographs corresponding to the cells shown in **c**. Scale bars, 100 µm (horizontal) and 10 min (vertical). **e**, Durotaxis quantification; $n = 33$ cells; two-tailed Mann-Whitney test; $^{**}P \leq 0.01$ (exact: $P = 0.0097$). **f-g**, Quantification of micropatterned PEG and BSA in microchannels with uniform and graded friction; $n = 10$ (PEG); $n = 9$ (BSA). Pale dots represent raw data; dark dots represent mean. **h**, Images of PLL-g-PEG/FITC and BSA-Alexa647 micropatterning (top panels), images of cells with a nuclear marker and pseudocoloured membrane at t=0 min and t=40 min (middle panels), and temporal colour-coded projected tracks (bottom panels). Scale bars, 50 µm. **i**, Kymographs corresponding to the cells shown in **h**. Cells were tracked via the nuclear marker. Scale bars, 50 µm (horizontal) and 10 min (vertical). **j**, Quantification of frictiotaxis index from $n = 74$ cells each; two-tailed Mann-Whitney test; $^{***}P \leq 0.001$ (exact: $P = 0.0010$).

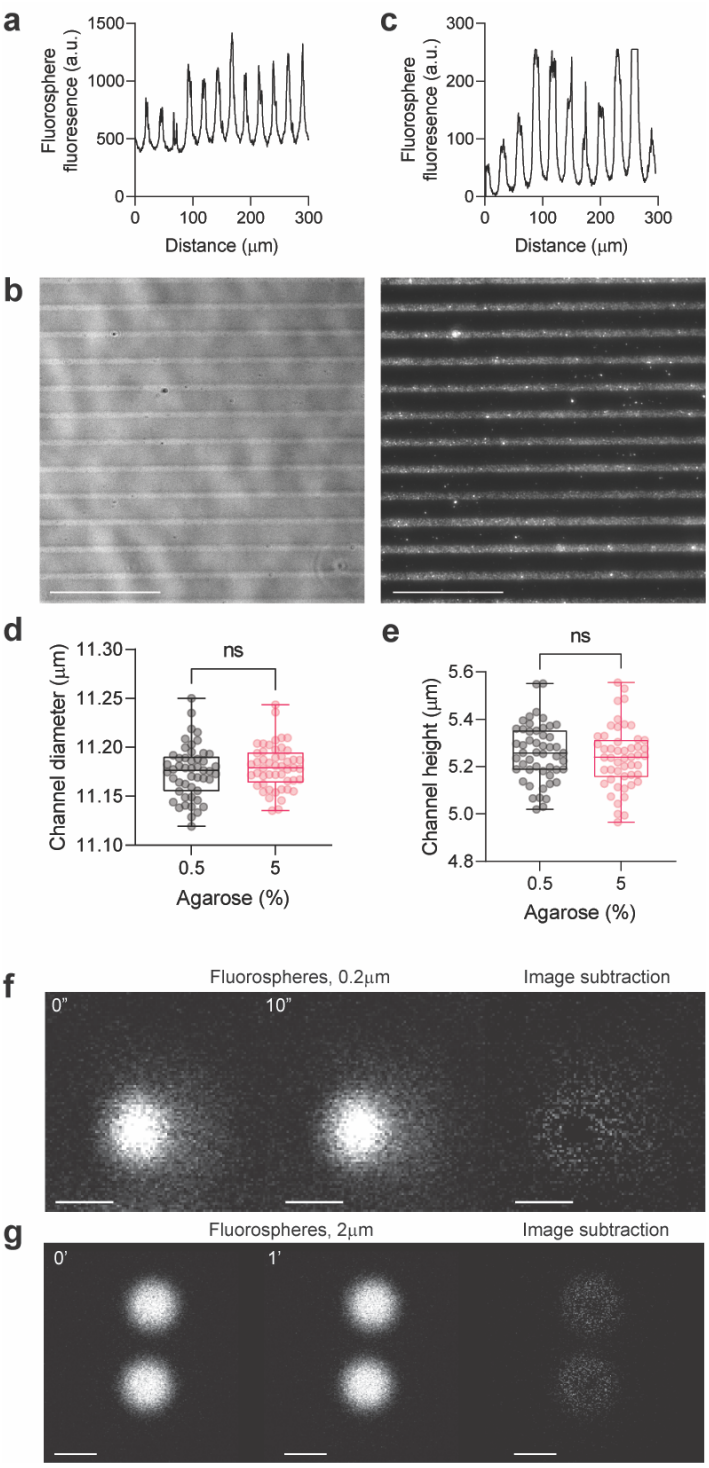

Extended Data Fig 1. The agarose microchannel assay. a-c, 5 μm agarose channels filled with 0.2 μm fluorospheres (**b**) and quantification along the orthogonal axis of fluorosphere-filled 10 μm (**c**) and 5 μm channels (**a**), as in Fig. 1c and Extended Data Fig. 1b, respectively. Scale bar, 100 μm. **d-e**, Channel dimensions quantified. Translucent dots represent individual data points. $N = 50$ channels; unpaired two-tailed t test; ns, $P>0.05$ (exact: $P=0.3482$ in **d**; $P=0.4649$ in **e**). **f-g**, 0.2 μm (**f**) or 2 μm fluorospheres (**g**) in 10 μm agarose microchannels at different time points. The right panel is an image subtraction between the images. Scale bar, 0.5 μm (**f**); 2 μm (**g**).

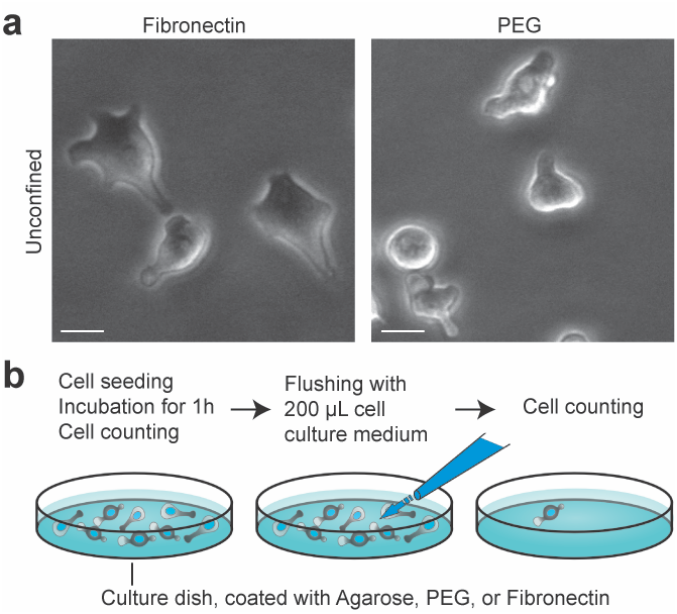

Extended Data Fig 2. Walker cells lack strong and specific adhesions. a, Pictures of cells in adhesive (fibronectin, left) or non-adhesive (PEG, right) conditions. Scale bar, 10 µm. **b**, Illustration depicting the principle and quantification of the flushing experiment.

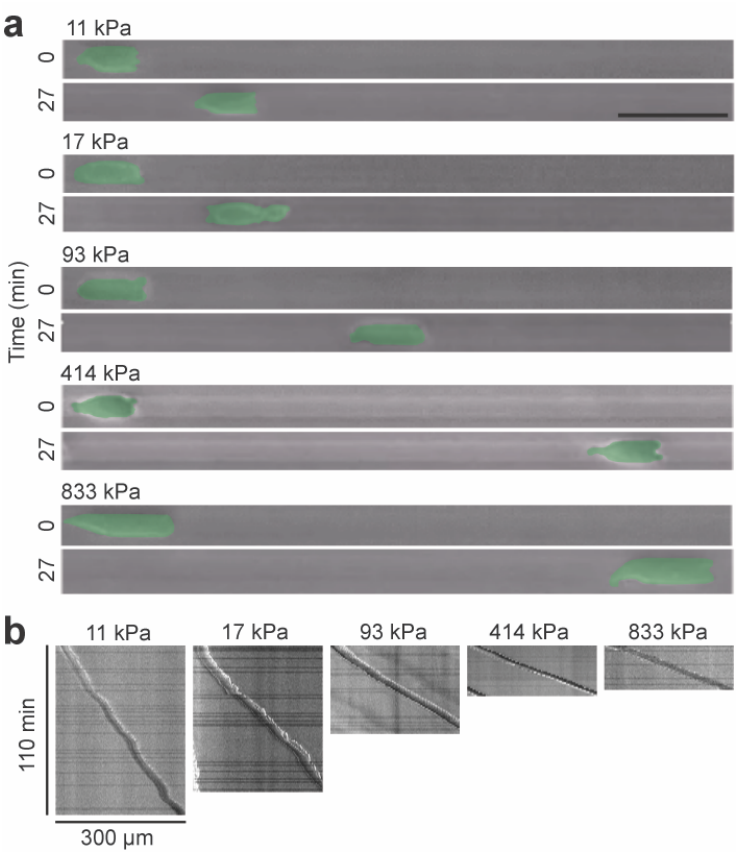

Extended Data Fig 3. Stiffness-dependent migration speed in microchannels. a, Pictures of cells with pseudocoloured membrane at early (t=0 min) and later (t=27 min) time points in microchannels of different stiffness regimes. Scale bar, 50 µm. **b**, Kymographs corresponding to the cells depicted in (**a**). Scale bars equal 300 µm (horizontal) and 110 min (vertical).

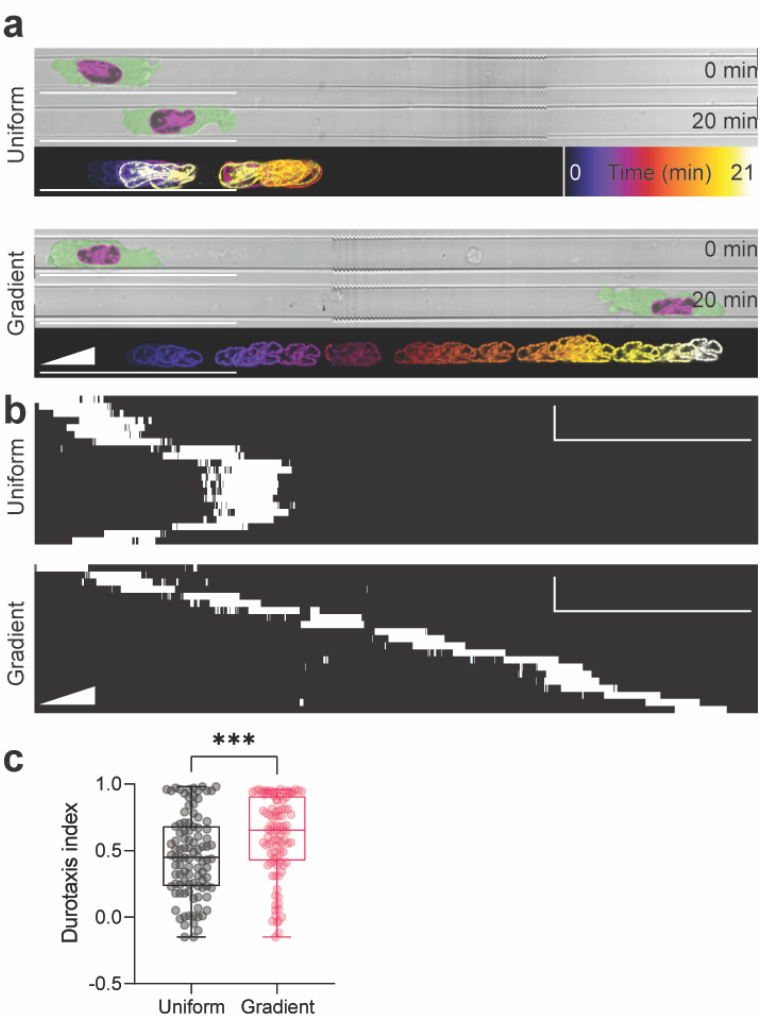

Extended Data Fig 4. Durotaxis of HL60 cells. a-b, Example cells at early and later time points (upper and middle panels, **a**), temporal colour-coded projections (bottom panels, **a**) and kymographs (**b**) in uniform and graded stiffness substrate. Cells were tracked by labelling the nucleus with Hoechst 33342 and the cell membrane was pseudocoloured. Images are stitched as described in the Methods. Scale bar, 50 µm. Vertical scale bar (**b**), 5 min. **c,** Durotaxis quantification. n = 100 cells; two-tailed Mann-Whitney test; ***$P \leq 0.001$ (exact: P=0.0006).

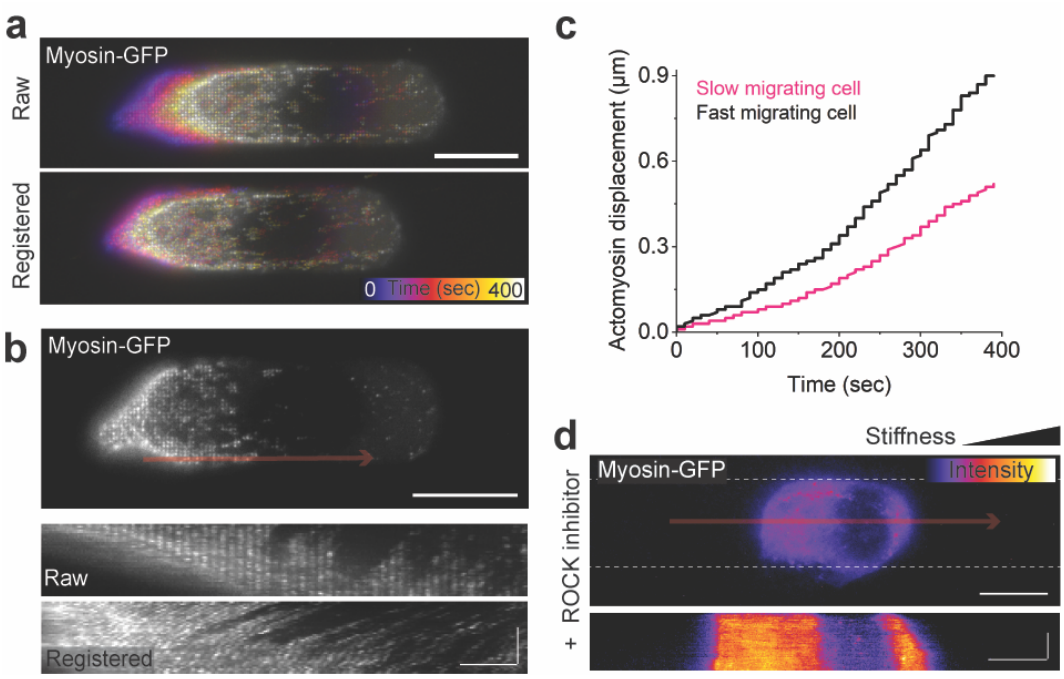

Extended Data Fig 5. Visualisation of retrograde actomyosin flow. a, Temporal colour-coded projection of a Myosin-GFP-expressing Walker cell before (raw_top panel) and after image registration (registered_bottom panel). Scale bar equals 10 µm. **b**, Kymographs of actomyosin flow, corresponding to the area along the red arrow in the upper panel, before (raw) and after image registration (registered). Scale bars, 10 µm in the upper panel; 5 µm (horizontal) and 200 s (vertical) in kymographs of lower panels. **c**, Examples of actomyosin displacement over time of a slow (1.47 µm/min) versus faster (2.16 µm/min) migrating cell in a microchannel with stiffness gradient. **d**, Colour-coded still image (upper panel) and Kymograph (lower panel, corresponding to the red arrow in the upper panel) of a Walker cell expressing Myosin-GFP, in a microchannel with stiffness gradient, and treated with 30 µM ROCK inhibitor (Y-27632). Dotted lines in the upper panel represent channel boundaries. Scale bars, 10 µm in upper panel; 10 µm (horizontal) and 20 min (vertical) in lower panel.

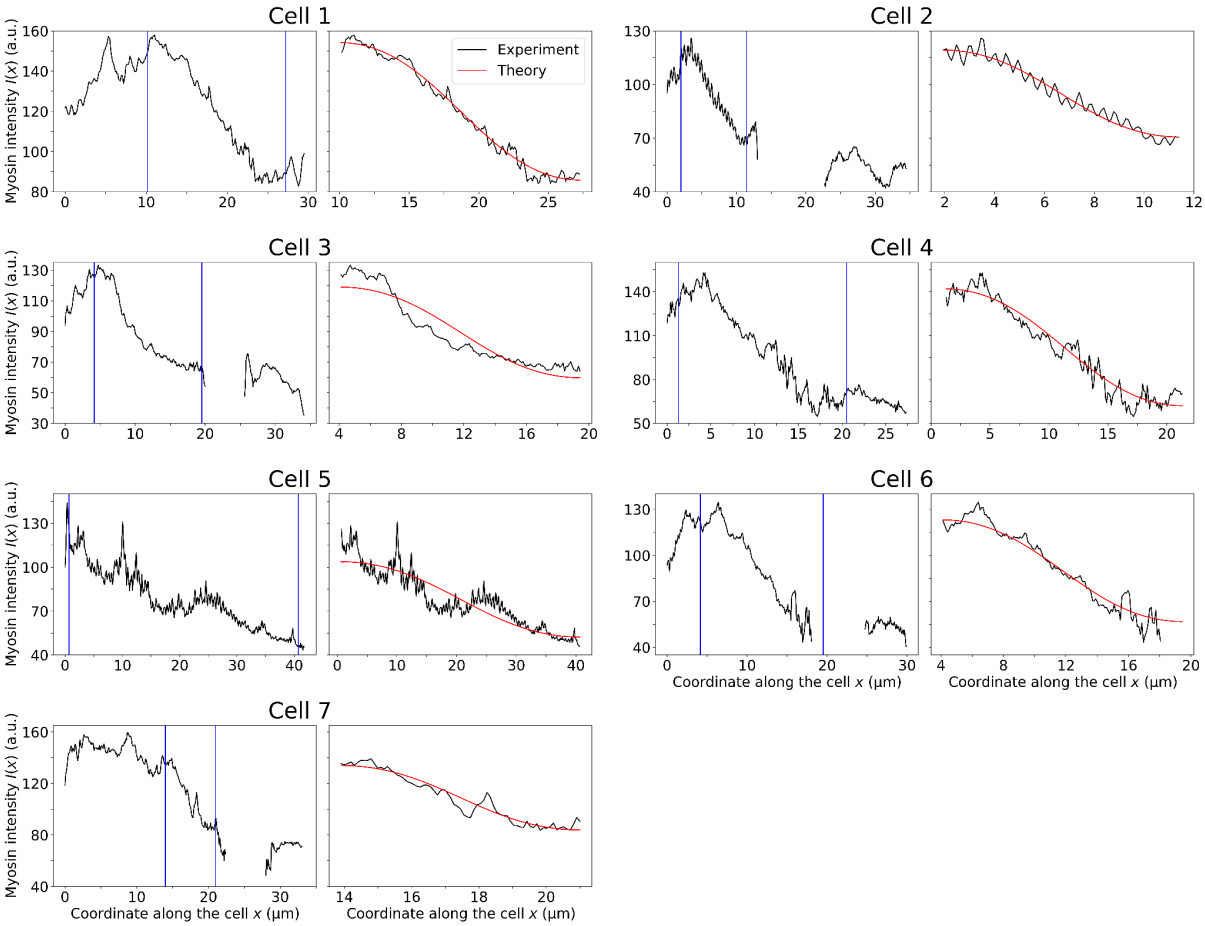

Extended Data Fig 6. Fits of the myosin intensity profiles for cells migrating on uniform friction. For each cell, the left column shows the myosin intensity profile along the cell at a single time frame. For some cells, there is missing intensity data at certain positions due to the nucleus displacing myosin. Only the data between the vertical blue lines is used for comparison to the steady-state solutions of the model. For each cell, the right column shows the fit of the steady-state solutions of the model (red) to the experimental data (black) selected from the left panels. Error bars are not visible as the errors of the mean of the experimentally measured intensities are typically around 1-5 a.u., which is much less than their absolute values. The fit parameter values are listed in Table I.

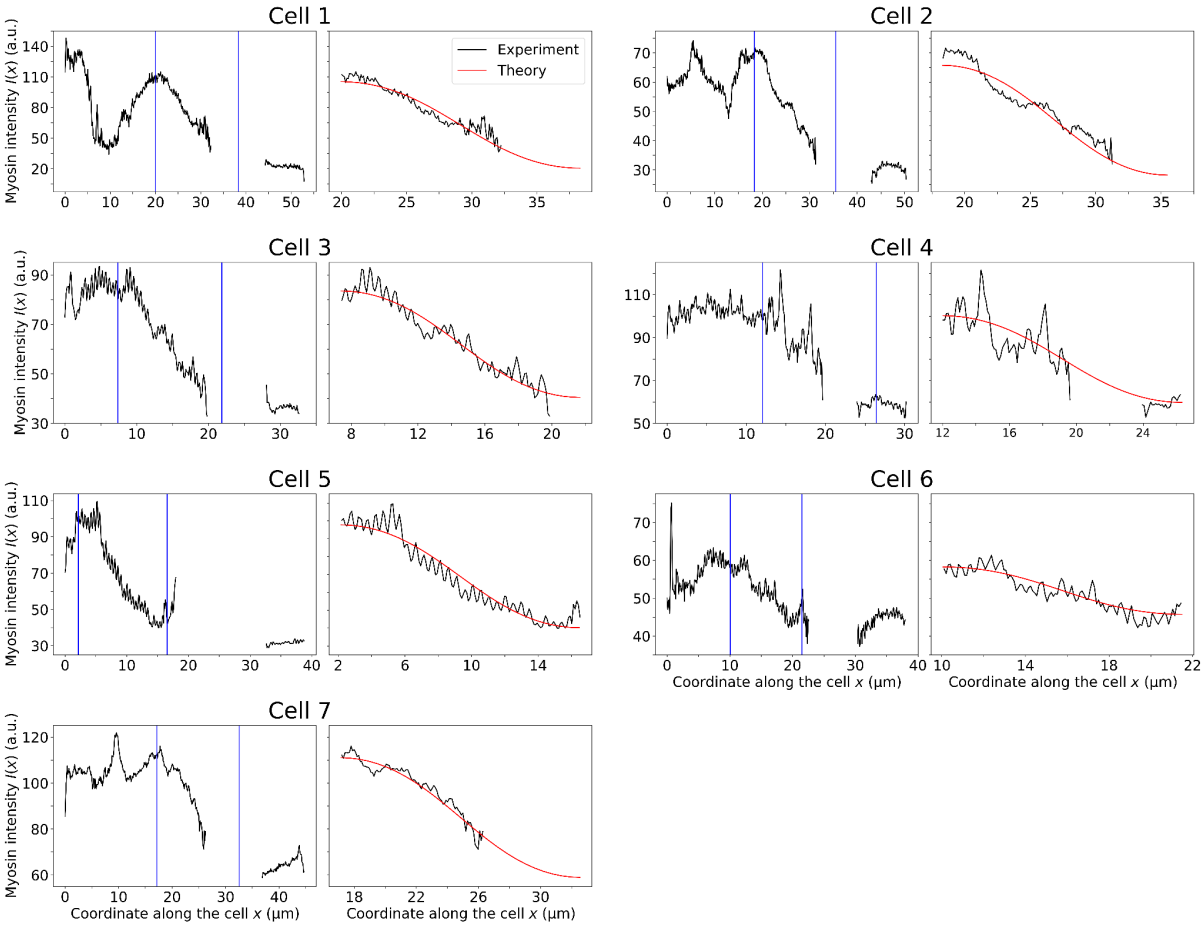

Extended Data Fig 7. Fits of the myosin intensity profiles for cells migrating on a friction gradient. For each cell, the left column shows the myosin intensity profile along the cell at a single time frame. For some cells, there is missing intensity data at certain positions due to the nucleus displacing myosin. Only the data between the vertical blue lines is used for comparison to the steady-state solutions of the model. For each cell, the right column shows the fit of the steady-state solutions of the model (red) to the experimental data (black) selected from the left panels. Error bars are not visible as the errors of the mean of the experimentally measured intensities are typically around 1-5 a.u., which is much less than their absolute values. The fit parameter values are listed in Table I.

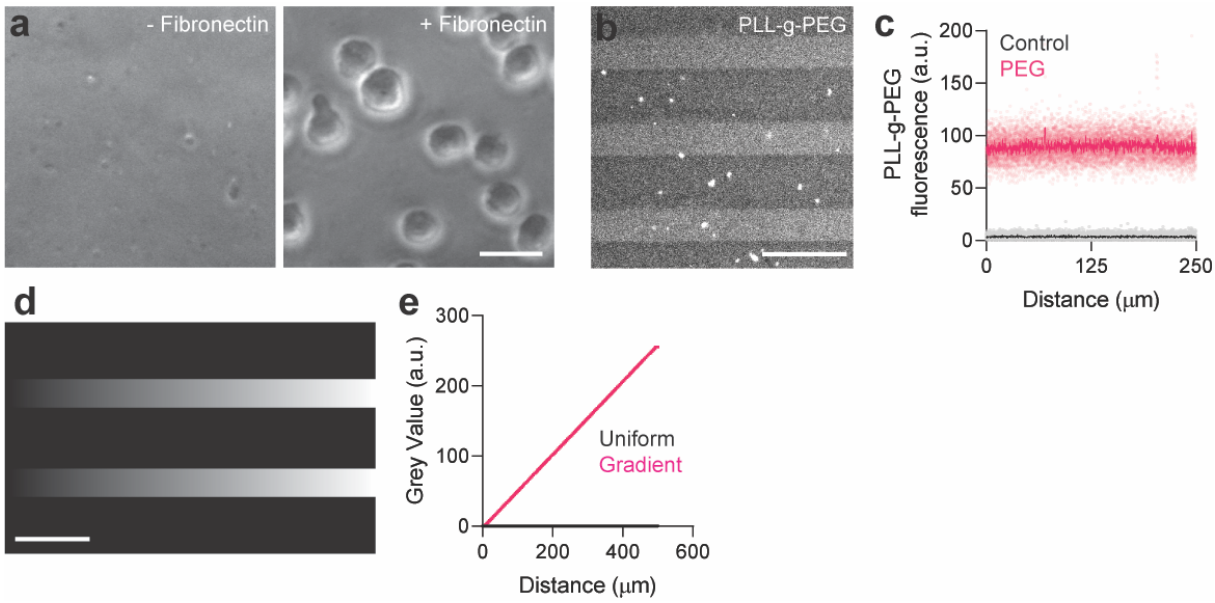

Extended Data Fig. 8 Agarose activation, PEG coating and photopatterning gradients for frictiotaxis experiments. a, Cells adhere to a fibronectin-coated agarose gel. Medium was aspirated and flushed several times to remove any cells in suspension. Scale bar, 20 μm. **b-c**, PLL-g-PEG/FITC-coated or uncoated (control) agarose microchannels (**b**) and quantification of fluorescence (**c**); $n = 10$; pale colours represent raw data; dark colours represent mean. Scale bar, 20 μm. **d**, The designed photopattern which exhibits alternating control and gradient masks. Scale bar, 100 μm. **e**, Quantification of (**d**).

	Uniform friction		Friction gradient	
Cell #	$I_0/10$	$\bar{\alpha}/10^2$	$I_0/10$	$\bar{\alpha}/10^2$
1	12.0 ± 0.5	2.6 ± 0.5	6.3 ± 0.2	0.5 ± 0.2
2	9.5 ± 0.4	3.3 ± 0.8	4.7 ± 0.2	1.3 ± 0.7
3	8.9 ± 0.4	2.0 ± 1.0	6.2 ± 0.3	1.8 ± 0.7
4	10.1 ± 0.5	1.4 ± 0.6	8.0 ± 0.7	3.0 ± 3.0
5	7.8 ± 0.4	2.0 ± 2.0	6.9 ± 0.4	1.2 ± 0.6
6	9.0 ± 0.5	2.0 ± 1.0	5.2 ± 0.1	14.0 ± 1.0
7	10.9 ± 0.4	4.0 ± 2.0	8.5 ± 0.3	2.2 ± 0.5

Table I. Fit parameter values. Values of the scaling factor I_0 and the pressure coefficient $\bar{\alpha}$ obtained from the fits shown in Extended Data Figs. 6-7, which correspond to 7 cells migrating on uniform friction and 7 cells migrating on a friction gradient, respectively.

460 **Supplementary Video 1. Agarose microchannel assay.**

461 Walker cells migrating within 10 µm width microchannels within a 1% agarose substrate.

462 Movie length, 481 min. Scale bar, 100 µm.

463

464 **Supplementary Video 2. Adhesion-independent durotaxis.**

465 Walker cells undergo durotaxis without strong or specific adhesions to the substrate. Movie

466 length, 40 min. Scale bar, 50 µm.

467

468 **Supplementary Video 3. Stiffness-dependent migration speed.**

469 Migration speed of Walker cells increases with higher substrate stiffness. Movie length, 110

470 min.

471

472 **Supplementary Video 4. Myosin rear accumulation in gradient and uniform stiffness.**

473 In stiffness gradient and uniform stiffness microchannels, Myosin-GFP accumulates at the

474 cell rear and accumulation switches to the opposite pole when cells repolarise.

475

476 **Supplementary Video 5. Retrograde Myosin-GFP flow in raw and registered sequences.**

477 Retrograde Myosin-GFP flow is observed in raw and registered timelapse sequences.

478

479 **Supplementary Video 6. Myosin inhibition abrogates migration in microchannels.**

480 Upper panel: DMSO control. Lower panel: 30 µM Y-27632. Note that both cells in the lower

481 panel do not form blebs and do not migrate.

482

483 **Supplementary Video 7. Frictiotaxis.**

484 Walker cells undergo frictiotaxis on PEG-BSA gradients. Movie length, 98 min. Scale bar, 50

485 µm.

References

1 Shellard, A. & Mayor, R. All Roads Lead to Directional Cell Migration. *Trends Cell Biol* **30**, 852-868 (2020). https://doi.org:10.1016/j.tcb.2020.08.002

2 SenGupta, S., Parent, C. A. & Bear, J. E. The principles of directed cell migration. *Nat Rev Mol Cell Biol* **22**, 529-547 (2021). https://doi.org:10.1038/s41580-021-00366-6

3 Shellard, A. & Mayor, R. Collective durotaxis along a self-generated stiffness gradient in vivo. *Nature* **600**, 690-694 (2021). https://doi.org:10.1038/s41586-021-04210-x

4 Shellard, A. & Mayor, R. Durotaxis: The Hard Path from In Vitro to In Vivo. *Dev Cell* **56**, 227-239 (2021). https://doi.org:10.1016/j.devcel.2020.11.019

5 Sunyer, R. *et al.* Collective cell durotaxis emerges from long-range intercellular force transmission. *Science* **353**, 1157-1161 (2016). https://doi.org:10.1126/science.aaf7119

6 Lo, C. M., Wang, H. B., Dembo, M. & Wang, Y. L. Cell movement is guided by the rigidity of the substrate. *Biophys J* **79**, 144-152 (2000). https://doi.org:10.1016/S0006-3495(00)76279-5

7 Koser, D. E. *et al.* Mechanosensing is critical for axon growth in the developing brain. *Nat Neurosci* **19**, 1592-1598 (2016). https://doi.org:10.1038/nn.4394

8 Pallarès, M. E. *et al.* Stiffness-dependent active wetting enables optimal collective cell durotaxis. *Nature Physics* **19**, 279-289 (2023). https://doi.org:10.1038/s41567-022-01835-1

9 Alert, R. & Casademunt, J. Role of Substrate Stiffness in Tissue Spreading: Wetting Transition and Tissue Durotaxis. *Langmuir* **35**, 7571-7577 (2019). https://doi.org:10.1021/acs.langmuir.8b02037

10 Isomursu, A. *et al.* Directed cell migration towards softer environments. *Nat Mater* **21**, 1081-1090 (2022). https://doi.org:10.1038/s41563-022-01294-2

11 Yamada, K. M. & Sixt, M. Mechanisms of 3D cell migration. *Nat Rev Mol Cell Biol* **20**, 738-752 (2019). https://doi.org:10.1038/s41580-019-0172-9

12 Bodor, D. L., Ponisch, W., Endres, R. G. & Paluch, E. K. Of Cell Shapes and Motion: The Physical Basis of Animal Cell Migration. *Dev Cell* **52**, 550-562 (2020). https://doi.org:10.1016/j.devcel.2020.02.013

13 Paluch, E. K., Aspalter, I. M. & Sixt, M. Focal Adhesion-Independent Cell Migration. *Annu Rev Cell Dev Biol* **32**, 469-490 (2016). https://doi.org:10.1146/annurev-cellbio-111315-125341

14 Moreau, H. D., Piel, M., Voituriez, R. & Lennon-Duménil, A.-M. Integrating Physical and Molecular Insights on Immune Cell Migration. *Trends in Immunology* **39**, 632-643 (2018). https://doi.org:https://doi.org/10.1016/j.it.2018.04.007

15 Liu, Y.-J. *et al.* Confinement and Low Adhesion Induce Fast Amoeboid Migration of Slow Mesenchymal Cells. *Cell* **160**, 659-672 (2015). https://doi.org:https://doi.org/10.1016/j.cell.2015.01.007

16 Ruprecht, V. *et al.* Cortical contractility triggers a stochastic switch to fast amoeboid cell motility. *Cell* **160**, 673-685 (2015). https://doi.org:10.1016/j.cell.2015.01.008

17 Guimarães, C. F., Gasperini, L., Marques, A. P. & Reis, R. L. The stiffness of living tissues and its implications for tissue engineering. *Nature Reviews Materials* **5**, 351-370 (2020). https://doi.org:10.1038/s41578-019-0169-1

18 Bergert, M. *et al.* Force transmission during adhesion-independent migration. *Nat Cell Biol* **17**, 524-529 (2015). https://doi.org:10.1038/ncb3134

19 Bergert, M., Chandradoss, S. D., Desai, R. A. & Paluch, E. Cell mechanics control rapid transitions between blebs and lamellipodia during migration. *Proc Natl Acad Sci U S A* **109**, 14434-14439 (2012). https://doi.org:10.1073/pnas.1207968109

20 Wilson, K. *et al.* Mechanisms of leading edge protrusion in interstitial migration. *Nat Commun* **4**, 2896 (2013). https://doi.org:10.1038/ncomms3896
21 Callan-Jones, A. Self-organization in amoeboid motility. *Front Cell Dev Biol* **10**, 1000071 (2022). https://doi.org:10.3389/fcell.2022.1000071
22 Reversat, A. *et al.* Cellular locomotion using environmental topography. *Nature* **582**, 582-585 (2020). https://doi.org:10.1038/s41586-020-2283-z
23 Callan-Jones, A. C. & Voituriez, R. Actin flows in cell migration: from locomotion and polarity to trajectories. *Curr Opin Cell Biol* **38**, 12-17 (2016). https://doi.org:10.1016/j.ceb.2016.01.003
24 Callan-Jones, A. C. & Voituriez, R. Active gel model of amoeboid cell motility. *New Journal of Physics* **15**, 025022 (2013). https://doi.org:10.1088/1367-2630/15/2/025022
25 Hawkins, R. J. *et al.* Spontaneous contractility-mediated cortical flow generates cell migration in three-dimensional environments. *Biophys J* **101**, 1041-1045 (2011). https://doi.org:10.1016/j.bpj.2011.07.038
26 Byun, S. *et al.* Characterizing deformability and surface friction of cancer cells. *Proc Natl Acad Sci U S A* **110**, 7580-7585 (2013). https://doi.org:10.1073/pnas.1218806110
27 Carlsson, J., Gabel, D., Larsson, E., Ponten, J. & Westermark, B. Protein-coated agarose surfaces for attachment of cells. *In Vitro* **15**, 844-850 (1979). https://doi.org:10.1007/BF02618038
28 Porath, J., Axen, R. & Ernback, S. Chemical coupling of proteins to agarose. *Nature* **215**, 1491-1492 (1967). https://doi.org:10.1038/2151491a0
29 Carlsson, A. E. Mechanisms of Cell Propulsion by Active Stresses. *New J Phys* **13** (2011). https://doi.org:10.1088/1367-2630/13/7/073009
30 Steimel, J. P., Aragones, J. L. & Alexander-Katz, A. Artificial tribotactic microscopic walkers: walking based on friction gradients. *Phys Rev Lett* **113**, 178101 (2014). https://doi.org:10.1103/PhysRevLett.113.178101
31 Gaertner, F. *et al.* WASp triggers mechanosensitive actin patches to facilitate immune cell migration in dense tissues. *Dev Cell* **57**, 47-62 e49 (2022). https://doi.org:10.1016/j.devcel.2021.11.024
32 Brunetti, R. M. *et al.* WASP integrates substrate topology and cell polarity to guide neutrophil migration. *J Cell Biol* **221** (2022). https://doi.org:10.1083/jcb.202104046
33 Renkawitz, J. *et al.* Nuclear positioning facilitates amoeboid migration along the path of least resistance. *Nature* **568**, 546-550 (2019). https://doi.org:10.1038/s41586-019-1087-5
34 Le Berre, M. *et al.* Geometric friction directs cell migration. *Phys Rev Lett* **111**, 198101 (2013). https://doi.org:10.1103/PhysRevLett.111.198101
35 Ding, Y., Xu, G. K. & Wang, G. F. On the determination of elastic moduli of cells by AFM based indentation. *Sci Rep* **7**, 45575 (2017). https://doi.org:10.1038/srep45575
36 Schiesser, W. E. & Griffiths, G. W. *A Compendium of Partial Differential Equation Models: Method of Lines Analysis with Matlab*. (Cambridge University Press, 2009).
37 Schiesser, W. E. *The Numerical Method of Lines: Integration of Partial Differential Equations*. (Elsevier Science, 2012).
38 Hamdi, S., Schiesser, W. & Griffiths, G. Method of lines. *Scholarpedia* **2**, 2859 (2007). https://doi.org:10.4249/scholarpedia.2859

583 **Materials and Methods**

584 Cell culture

585 Walker 256 carcinosarcoma cells (RRID:CVCL_4984), Walker myosin light chain-GFP
586 cells, and Walker Lifeact-GFP cells were a gift from E. Paluch (University of Cambridge,
587 UK). Walker cells and HL60 cells (RRID:CVCL_0002) were grown in T-25 suspension cell
588 culture flasks (Sarstedt, 83.3910.502) in RPMI 1640 media containing L-glutamine (Gibco,
589 11875101) supplemented with 10% heat-inactivated FCS and 1% penicillin-streptomycin
590 (Gibco, 10378016) at 37°C and 5% CO_2. The culture media for the HL60 cells additionally
591 contained 40 mM Hepes for buffering. Differentiation of HL60 cells was achieved by
592 incubating cells in propagation media plus 1.3% DMSO for 5 days. All working media was
593 passed through 0.2 µm Sartorius Minisart filters (VWR, 611-0691) prior to use. For
594 experiments, cells were transferred to media identical to their culture media except lacking
595 FCS. For myosin inhibition experiments, the imaging medium was additionally supplemented
596 with 30 µM of the ROCK inhibitor Y-27632 (Selleckchem, S6390), and an equivalent
597 volume of DMSO was added to the control condition. Cells were allowed to equilibrate in the
598 medium for 30 min before the start of the experiment.

599 Where appropriate, cells were labelled with Hoechst 33342 (Leica, H3570) at $1x10^{-5}$ mg/mL,
600 or BioTracker 490 Green Cytoplasmic Membrane Dye (Merck, SCT106) at 5 µL per 1 mL
601 cell suspension. In both cases, a concentrated cell solution was incubated with the marker for
602 30 min at 37°C before being washed out. Immunostaining against phospho-paxillin Tyr 118
603 (ThermoFisher, 44-722G) was performed by fixing in 4% paraformaldehyde for 10 min at
604 37°C followed by 0.1% Triton X-100 permeabilization for 15 min at RT, blocking in 2%
605 BSA/PBS for 1 hour at RT, 1:1000 primary antibody overnight at 4°C and a AlexaFluor goat
606 anti-rabbit secondary antibody (ThermoFisher, A-11008) at 1:500 for 4 hours at RT with PBS
607 washes in between antibody steps.

608

609 Image processing, data analysis and statistics

610 Images and videos were processed using Fiji. Cells were tracked using the Manual Tracking
611 plugin, and output data processed in the Chemotaxis and Migration Tool (Ibidi, Version 2.0).
612 In this manuscript, we have named Forward Migration Index as the Durotaxis Index, where
613 the axis of interest is along the stiffness gradient and where positive values indicate
614 straightness toward stiff substrate, and negative values indicate straightness toward soft
615 substrate.

616 To achieve high resolution imaging of cells across large regions, images were stitched for
617 analysis and presentation. Correction for uneven illumination was performed where
618 appropriate. Cells in contact with other cells were not included in the analysis, and tracks
619 were cut short where cell-cell contacts were made, to ensure only single cell analysis was
620 performed.

621 To quantify retrograde actomyosin flow independently from cell displacement, linear stack
622 alignment with SIFT was carried out in Fiji, and displacement was tracked manually in
623 kymographs, using the segmented line tool.

624 Normality in the spread of data for each experiment was tested using the Kolmogorov-
625 Smirnov, d'Agostino-Pearson, and Shapiro-Wilk tests in Prism9 (GraphPad9). Significances
626 for datasets displaying normal distributions were calculated in Prism9 with paired or unpaired
627 two-tailed Student's *t*-tests or Mann-Whitney U tests where appropriate. No predetermination
628 of sample sizes were done. Cells were allocated into experimental groups randomly. Authors
629 were not blinded because cells were selected prior to analysis. Criteria for selection was
630 survival and not interacting with other cells. All experiments were replicated three times
631 (biological replicates) unless otherwise indicated.

632

633 Nanoindentation

634 Stiffness measurements were performed using nanoindentation (Chiaro, Optics11Life, Piuma
635 V2 v3.4.3) as previously described[3]. Cantilevers were customized by Optics11 Life. Probes
636 had a spherical glass tip with a radius of ~ 10 µm mounted onto an individually calibrated
637 cantilever with a spring constant of ~ 0.25 N m^{-1}. Deformation of the cantilever after contact
638 with the sample was measured by tracking the phase-shift in light, reflected from the back of
639 the cantilever. Samples were indented to a depth of 0.5 µm with a velocity of 2.5 µm s^{-1}. The
640 tip was held at this indentation depth for 1 s and then retracted over 1 s. The Young's moduli
641 were calculated automatically by the software by fitting the force versus indentation curve to
642 the linear Hertzian contact equation model[35]. The effective Young's modulus (E), referred to
643 in this manuscript as stiffness, is derived from the fit of the loading force-displacement curve
644 ($F(h)$), the indenter tip radius (R), and the indentation depth (h), according to the following
645 formula, for which a Poisson's ratio (v) of 0.5 was assumed, and was calculated automatically
646 by the software (Chiaro, Optics11Life, Piuma V2 v3.4.3).

647 $$F = \frac{4}{3} K \sqrt{r} \delta^{\frac{3}{2}} = \frac{4}{3} \frac{E}{1 - v^2} \sqrt{r} \delta^{\frac{3}{2}}$$

648

649 Atomic force microscopy

650 10 µm polystyrene beads were glued onto tipless MLCT B cantilevers (nominal spring
651 constant 0.02 N/m) and friction measurements were performed on the Nanowizard 4 AFM
652 system (Bruker Nano GmbH, JPK BioAFM) using Contact Mode. Lateral force was recorded
653 by sweeping the cantilever over a line of 10 µm length at a speed of 2.5 µm/s. We measured
654 the force at 5 kHz over a time frame of approximately 60 seconds to record several
655 oscillations. For each gel forces of 0.25, 0.5, 0.75, 1, 1.25, 1.5 and 1.75 nN was applied and
656 repeated at each force 5 times.

657

658 Micropatterning

659 PDMS or glass was plasma treated (Diener electronic) for 2 min and immediately coated with
660 100 µg/ml PLL(20)-g[3.5]-PEG(2) (Susos) or PLL(20)-g[3.5]-PEG(2)/FITC (Susos),
661 dissolved in PBS, for 30 min at room temperature. Surfaces were washed with 100 mM
662 Hepes pH 8-8.5 for 1h at room temperature and then incubated with 100 mg/ml mPEG-SVA
663 (Laysan Bio, MPEG-SVA-5000). Surfaces were washed in 1x PBS, followed by water, and
664 then air dried. The photoactivatable reagent, PLPP gel (Alvéole) was added at a ratio of 3:17
665 with 70% ethanol, at 1 µl PLPP gel/cm^2, and allowed to dry completely whilst protected from
666 light.

667 PRIMO (Alvéole) was calibrated with a 20x objective on a Nikon Ti inverted microscope
668 using Leonardo software (Alvéole). A greyscale pattern was used as shown in Extended Data
669 Fig. 8d. A dose of 30 mJ/mm^2 was used and laser power adjusted such that the patterning
670 time for each element was 4 s.

671 After patterning, the surface was washed several times with water and re-hydrated with PBS
672 for 5 min. The sample was then incubated with 50 µg/ml AlexaFluor647-conjugated BSA
673 (Thermo Fisher, A34785) overnight at 4°C prior to washing with PBS. Subsequent stages of
674 PDMS bonding to glass and imaging were performed as described in the Methods sections,
675 Soft lithography, and Imaging.

676

677 Photolithography

678 3-inch silicon wafers (Silicon wafer test grade, N(Phos), WAFER-SILI-0580W25 from PI-
679 KEM Ltd.) were plasma cleaned for 10 min at 100% power in a plasma cleaner (Henniker
680 Plasma HPT 100), and then baked on a hot plate at 200°C for 20 min to remove moisture.
681 After 10 s of cooling, SU-8 2005 (Kayaku Advanced Materials, purchased from A-Gas
682 Electronics Materials) was spin coated on the wafer at 500 rpm with an acceleration of 100

683 rpm s^{-1} for 30 s. After 2 min rest, the wafer was soft baked at 65°C for 1 min, followed by
684 95°C for 2 min, and then allowed to cool for 10 s. Writing was performed on a MicroWriter
685 ML3 using a 20x objective. Post-exposure bakes of the wafer were then performed at 65°C
686 for 1 min, 95°C for 2 min and then 65°C for 1 min. After 10 s cooling, the wafer was
687 developed in PGMEA (Sigma-Aldrich 484431-1L) for 1 min with manual agitation, before
688 rinsing in IPA for 10 s, dried with compressed N_2 and hard baked for 20 min at 200°C.
689 Dimensions of the wafer were analysed on an optical profiler (Sensofar S Neox).
690
691 Soft lithography
692 PDMS was made using reagents from a SYLGARD 184 Elastomer Kit (VWR, 634165S).
693 Base elastomer was thoroughly mixed with curing agent at a ratio of a ratio of 10:1, before
694 degassing in a vacuum desiccator (Scienceware, 999320237) with a KNF Laboport N96
695 diaphragm vacuum pump (Merck, Z675091-1EA). A Si wafer with positive features was
696 placed in a disposable aluminium dish (VWR, 611-1377), covered in PDMS, and baked for
697 10 min at 110°C. The PDMS was separated from the wafer and trimmed using a blade.
698
699 Agarose microchannels
700 PDMS was prepared as above, and spin coated onto a Si wafer with negative features using a
701 spin coater (Spin150) at conditions of 400 rpm for 30 s. The wafer was then baked at 110°C
702 for 10 min. The thin PDMS was peeled off from the wafer and cut into smaller pieces using a
703 razor blade, where each individual piece contained between one and four patterned designs.
704 To fabricate agarose microchannels, an individual PDMS piece was placed on a glass slide
705 with an edge aligned with the edge of the slide. A vacuum, and subsequently finger pressure,
706 was used to push trapped air bubbles out from underneath the PDMS. A ~1 mm thick piece of
707 PDMS was cut to generate a U-shape and placed around the PDMS pattern on the slide. A

708 coverslip was placed on top of the U-shape PDMS and neodymium magnets above the
709 coverslip and below the slide were used to secure the sandwich in place.
710 UltraPure low melting point agarose (ThermoFisher, 16520050) – in this manuscript referred
711 to as 'agarose' – was dissolved in RPMI media at the appropriate concentration, depending
712 on the experiment. The solution was maintained at 70ºC while penicillin-streptomycin
713 (Gibco, 10378016) was added to a final concentration of 1%. To fabricate gels of uniform
714 stiffness, the agarose solution was pipetted into the sandwich until full. To fabricate gels of
715 graded stiffness, higher concentration agarose solution (4%) was pipetted into the sandwich
716 mid-way, followed by lower concentration agarose solution (1%) until full. The gradient was
717 modulated by modifying the diffusion rate, which could be controlled by incubating in an
718 oven at different temperatures, angles and by modifying the input solutions. To solidify the
719 agarose gels, the sandwich was transferred to a 4ºC fridge. Afterwards, the sandwich was
720 disassembled and the solidified agarose slowly slid away from the underlying PDMS mould,
721 and reversed in orientation such that the structured agarose was face up. The surface was then
722 dried with a nitrogen gun and trimmed to size with a razorblade. The stiffness of agarose gels
723 was measured using a Chiaro nanointender (Methods, nanoindentation).
724 Holes were punched using a Harris uni-core 3 mm biopsy puncher (VWR, 89022-356),
725 followed by air drying with a nitrogen gun. A glass coverslip was then plasma cleaned and
726 bonded to the agarose microchannel chip, with the channels facing the coverslip. RPMI
727 media was pipetted into the holes and the unit placed in a humid chamber at 37°C and 5%
728 CO_2 for 30 min. The wells were then emptied using a p200 pipette and replaced with
729 concentrated cell solution. A 0.5 g weighted glass slide was placed on top of the structure,
730 and the unit placed in the stage of an inverted microscope.
731 Where appropriate, agarose surfaces were covalently bound to protein by using the CNBr-
732 method that has been reported previously[27,28]. After drying, agarose microchannels were

activated with cyanogen bromide: 50 mg/ml in water was mixed in an equal ratio with 0.5 M Na_2CO_3 in NaOH buffer, pH 11, which contained the protein (fibronectin or PLL-g-PEG). After 30 min, the surface was washed with water and then with the coupling buffer: 0.1 M sodium borate buffer, pH 8.5 for 4 h.

Measuring the myosin intensity profile

Fluorescent live cell imaging was performed on a ZEISS Elyra 7 microscope equipped with a 40×, NA = 1.2 water-immersion objective and operating in laser WF mode. Time series of single plane images along the cell-agarose interface were acquired in intervals of 10s. To prevent GFP quenching, RPMI medium without phenol red (Thermo Fisher, 11835030) was used in all experiments. Images were exported as TIF series for further analysis.

The experimental snapshots showed an intense myosin-GFP signal across the entire cell area except for the nuclear region. We cropped individual snapshots by hand using Fiji to exclude the background and nuclear region. We averaged the pixel intensities along the axis perpendicular to the direction of motion to obtain a one-dimensional intensity profile $I(x)$ along the cell.

Numerical solution of the active gel model for amoeboid migration

To reduce the number of free parameters, we simplified the model. Firstly, we assumed that the friction coefficient was constant. The equations in the model can be made independent of the equilibrium volume fraction ϕ_0. This can be seen by rescaling the gel volume fraction $\phi \to \phi_0\phi$, the pressure coefficient $\alpha \to \alpha/\phi_0^2$ and the drag coefficient $\xi_\mathrm{f} \to \xi_\mathrm{f}\phi_0$. We therefore set $\phi_0 = 1$ without loss of generality. Finally, we made Eqs. S13-16 in the Supplementary Note dimensionless as in Reference[24]. In dimensionless form, the model contains 4 dimensionless parameters: the active stress coefficient $\bar{\zeta} = \zeta L^2/\gamma$, the

758 depolymerization rate $\bar{k}_{\mathrm{d}} = k_{\mathrm{d}}\xi L^4/\gamma$, the pressure coefficient $\bar{\alpha} = \alpha L^2/\gamma$, and the drag

759 coefficient $\bar{\xi}_{\mathrm{f}} = \xi_f/(\xi L)$.

760 We solved the dimensionless equations using the Method of Lines[36-38] to predict the time

761 variation of the steady-state gel volume fraction profile $\phi_{\mathrm{ss}}(x,t)$ and the cell velocity $V(t)$

762 for migrating cells. We used centered finite differences to approximate the spatial derivatives.

763 Fictitious points were added outside the domain to define the spatial derivatives at the

764 boundaries. We used an explicit Euler step for the equations involving a time derivative and

765 we solved the remaining equations algebraically. We used 25-35 discretization points and a

766 time step of $\Delta t = 10^{-7}$. As initial conditions, we took the homogeneous state $\phi(x) = \phi_0$ plus

767 a small Gaussian-noise perturbation to each variable. The algorithm converges to provide a

768 steady-state gel volume fraction $\phi_{\mathrm{ss}}(x)$ and the corresponding cell velocity V_{ss}.

769

770 <u>Fitting the model to the myosin intensity profiles</u>

771 We take the myosin intensity profile $I(x)$ from the experimental images as a proxy for the

772 concentration of the actomyosin cortex, given by its steady-state volume fraction $\phi_{\mathrm{ss}}(x)$ in

773 the active gel model. However, we first had to select the region of the myosin intensity

774 profile that can be captured by the active gel model, given its assumptions. The model

775 captures cortical flow from low to high cortex concentrations and it assumes that the

776 concentration gradient vanishes at the rear and front of the cell. In contrast, experimental

777 myosin intensity profiles typically show extended intensity plateaus at each end of the cell,

778 which are connected by an intermediate intensity decay. To match the boundary conditions of

779 the model, we cropped the myosin intensity profiles to include only the intermediate decay

780 region and a small connected region of each plateau. In some cases, the myosin intensity at

781 the start of the plateau is obscured by the nucleus, so we roughly inferred where to crop the

782 profile by extrapolation. Also, cells 1 and 2 in Extended Data Fig. 6 have pronounced

783 uropods, which are myosin-rich tail structures that manifest as a second peak in the myosin
784 intensity profile at the rear side. We did not include the region of the uropod in the
785 comparison to the model. We indicate which region of each myosin intensity profile is
786 selected by means of vertical blue lines in Extended Data Figs. 6-7 (left-hand panels for each
787 cell).
788 We also had to scale the dimensions of the gel volume fraction $\phi(x)$ so that it could be
789 directly compared to the myosin intensity profile $I(x)$ in the selected region. The coordinate
790 along the cell was scaled linearly as $x \to xL$ to match the length L of the selected region.
791 Respectively, to fit it to the myosin intensity profile $I(x)$, we scaled the gel volume fraction
792 as $I(x) = I_0\phi_{\mathrm{ss}}(x)$, where I_0 is an additional free parameter in the fit.
793 Before performing the fits, we reduced the number of free parameters in the model. Firstly,
794 we fixed some of them: $\bar{\zeta} = 14$, $\bar{k}_{\mathrm{d}} = 1$, and $\bar{\xi}_{\mathrm{f}} = 0.46$. These parameter values ensure that
795 the homogeneous state is only unstable to perturbations with a wavelength given by the cell
796 length. As a result, in this parameter regime, the model has steady-state gel volume fraction
797 solutions $\phi_{\mathrm{ss}}(x)$ that decrease monotonically from the rear to the front of the cell. In addition,
798 each solution has an average value of gel volume fraction that is close to the equilibrium gel
799 volume fraction $\phi_0 = 1$. Therefore, for each snapshot, we calculated I_0 by measuring the
800 average myosin intensity in the selected region. In some cases, there was missing intensity
801 data in part of the selected region, due to the nucleus obscuring the myosin signal. Therefore,
802 we removed the intensity data at the opposite side of the selected region in calculating I_0,
803 which would otherwise skew the result.
804 By varying $\bar{\alpha}$, we performed a least-squares fit of the scaled steady-state volume fraction to
805 the myosin intensity profile in the selected region for each cell at a single time frame. We
806 show the fits in Extended Data Figs. 6-7 (right hand panels for each cell), and the
807 corresponding parameter values in Table I.

808 **Acknowledgements**

809 We thank E. Paluch for gifting us Walker 256 carcinosarcoma cells, L. Alvizi for advice with
810 tissue culture and J. Hartmann for assistance with stitching. We thank P. Saez for advice
811 about PDMS and microchannels. We thank Alveole and Cairn for providing access to the
812 PRIMO, as well as P. March for access to the PRIMO at the University of Manchester. P.H.
813 and R.A. thank A. Callan-Jones, P. Haas, and J. Neipel for discussions on the model and M.
814 Bovyn for discussions on the fits.

815

816 **Funding**

817 Work in the laboratory of R.M. is supported by grants from the Medical Research Council
818 (MR/S007792/1), Biotechnology and Biological Services Research Council (M008517;
819 BB/T013044) and Wellcome Trust (102489/Z/13/Z). K.W. is supported by the Deutsche
820 Forschungsgemeinschaft (DFG) via the Walter Benjamin Fellowship (WE 7331/1-1).

821

822 **Author contributions**

823 A.S. and K.W. conceived the project, performed the experiments, and analysed the
824 experimental data. R.A. and P.H. developed the physical model and derived the explanation of
825 frictiotaxis. P.H. solved the model numerically and fitted it to the experimental data. N.S.
826 contributed to conceptualisation of the model and performed AFM with R.T. with assistance
827 from G.C. G.C. provided conceptual and technical advice, especially with AFM and tissue
828 culture. A.S and C.D. generated the silicon wafers in A.I.'s laboratory. A.S., K.W., R.M. and
829 R.A. wrote and edited the manuscript. All authors commented on the manuscript.

830

831 **Competing interests**

832 The authors declare that they have no competing interests.

Data and materials availability

All data are available in the main text or the supplementary materials.